Draft version February 7, 2023
Typeset using LaTeX twocolumn style in AASTeX631

A candidate runaway supermassive black hole identified by shocks and star formation in its wake

Pieter van Dokkum,[1] Imad Pasha,[1] Maria Luisa Buzzo,[2] Stephanie LaMassa,[3] Zili Shen,[1] Michael A. Keim,[1] Roberto Abraham,[4] Charlie Conroy,[5] Shany Danieli,[6,*] Kaustav Mitra,[1] Daisuke Nagai,[7] Priyamvada Natarajan,[1] Aaron J. Romanowsky,[8,9] Grant Tremblay,[5] C. Megan Urry,[7] and Frank C. van den Bosch[1]

[1] *Astronomy Department, Yale University, 52 Hillhouse Ave, New Haven, CT 06511, USA*
[2] *Swinburne University of Technology, Melbourne, Victoria, Australia*
[3] *Space Telescope Science Institute, 3700 San Martin Drive, Baltimore, MD 21218, USA*
[4] *Department of Astronomy & Astrophysics, University of Toronto, 50 St. George Street, Toronto, ON M5S 3H4, Canada*
[5] *Harvard-Smithsonian Center for Astrophysics, 60 Garden Street, Cambridge, MA, USA*
[6] *Department of Astrophysical Sciences, 4 Ivy Lane, Princeton University, Princeton, NJ 08544, USA*
[7] *Department of Physics, Yale University, P.O. Box 208121, New Haven, CT 06520, USA*
[8] *Department of Physics and Astronomy, San José State University, San Jose, CA 95192, USA*
[9] *Department of Astronomy and Astrophysics, University of California Santa Cruz, 1156 High Street, Santa Cruz, CA 95064, USA*

ABSTRACT

The interaction of a runaway supermassive black hole (SMBH) with the circumgalactic medium (CGM) can lead to the formation of a wake of shocked gas and young stars behind it. Here we report the serendipitous discovery of an extremely narrow linear feature in HST/ACS images that may be an example of such a wake. The feature extends 62 kpc from the nucleus of a compact star-forming galaxy at $z = 0.964$. Keck LRIS spectra show that the [O III]/Hβ ratio varies from ~ 1 to ~ 10 along the feature, indicating a mixture of star formation and fast shocks. The feature terminates in a bright [O III] knot with a luminosity of $\approx 1.9 \times 10^{41}$ ergs s^{-1}. The stellar continuum colors vary along the feature, and are well-fit by a simple model that has a monotonically increasing age with distance from the tip. The line ratios, colors, and the overall morphology are consistent with an ejected SMBH moving through the CGM at high speed while triggering star formation. The best-fit time since ejection is ~ 39 Myr and the implied velocity is $v_{\rm BH} \sim 1600\,{\rm km\,s^{-1}}$. The feature is not perfectly straight in the HST images, and we show that the amplitude of the observed spatial variations is consistent with the runaway SMBH interpretation. Opposite the primary wake is a fainter and shorter feature, detected only in [O III] and the rest-frame far-ultraviolet. This feature may be shocked gas behind a binary SMBH that was ejected at the same time as the SMBH that produced the primary wake.

1. INTRODUCTION

There are several ways for a supermassive black hole (SMBH) to escape from the center of a galaxy. The first step is always a galaxy merger, which leads to the formation of a binary SMBH at the center of the merger remnant (Begelman et al. 1980; Milosavljević & Merritt 2001). The binary can be long-lived, of order $\sim 10^9$ yr, and if a third SMBH reaches the center of the galaxy before the binary merges, a three-body interaction can impart a large velocity to one of the SMBHs leading to its escape from the nucleus (Saslaw et al. 1974; Volonteri et al. 2003; Hoffman & Loeb 2007). Even in the absence of a third SMBH, the eventual merger of the binary can impart a kick to the newly formed black hole through gravitational radiation recoil (Bekenstein 1973; Campanelli et al. 2007). The velocity of the ejected SMBH depends on the mechanism and the specific dynamics. Generally the kicks are expected to be higher for slingshot scenarios than for recoils (see, e.g., Hoffman & Loeb 2007; Kesden et al. 2010), although in exceptional cases recoils may reach $\sim 5000\,{\rm km\,s^{-1}}$ (Campanelli et al. 2007; Lousto & Zlochower 2011). In both scenarios the velocity of the SMBH may exceed the escape velocity of the host galaxy (see, e.g., Saslaw et al. 1974; Hoffman & Loeb 2007; Lousto et al. 2012; Ricarte et al. 2021b).

Identifying such runaway SMBHs is of obvious interest but difficult. The main focus has been on the special case where the black hole is accreting at a high enough rate to be identified as a kinematically or spatially displaced active galactic nucleus (AGN) (Bonning et al. 2007; Blecha et al. 2011; Komossa 2012). For such objects, the presence of a SMBH is not in doubt, but it can be difficult to determine whether they are "naked" black holes or the nuclei of merging galaxies (see, e.g., Merritt et al. 2006). Candidates include the peculiar double X-ray source CID-42 in the COSMOS field

* NASA Hubble Fellow

(Civano et al. 2010) and the quasars HE0450–2958 (Magain et al. 2005), SDSSJ0927+2943 (Komossa et al. 2008), E1821+643 (Robinson et al. 2010; Jadhav et al. 2021), and 3C 186 (Chiaberge et al. 2017).

Quiescent (non-accreting) runaway SMBHs can be detected through the effect they have on their surroundings. As noted by Boylan-Kolchin et al. (2004) and discussed in-depth by Merritt et al. (2009), some of the stars in the nuclear regions of the galaxy are expected to remain bound to the SMBH during and after its departure. The stellar mass that accompanies the black hole is a steeply declining function of its velocity, and generally $\lesssim M_{\rm BH}$. This leads to peculiar objects, dubbed "hyper compact stellar systems" (HCSS) by Merritt et al. (2009), with the sizes and luminosities of globular clusters or ultra compact dwarf galaxies but the velocity dispersions of massive galaxy nuclei. HCSSs could therefore be easily identified by their kinematics, but measuring velocity dispersions of such faint objects is difficult beyond the very local Universe. Other potential detection methods include gravitational lensing (Sahu et al. 2022) and tidal disruption events (e.g., Ricarte et al. 2021a; Angus et al. 2022). No convincing candidates have been found so far.

Another way to identify runaway SMBHs is through the effect of their passage on the surrounding gas. This topic has an interesting history as it is rooted in AGN models that turned out to be dead ends. Saslaw & De Young (1972) investigated the suggestion by Burbidge et al. (1971) and Arp (1972) that the redshifts of quasars are not cosmological but that they were ejected from nearby galaxies. In that context they studied what happens when a SMBH travels supersonically through ionized hydrogen, finding that this produces a shock front with a long wake behind it. Shocked gas clouds in the wake can cool and form stars, potentially illuminating the wake with ionizing radiation from O stars. Rees & Saslaw (1975) analyzed the possibility that double radio sources are produced by the interaction of escaped SMBHs with the intergalactic gas. They find that this is plausible from an energetics standpoint, although now we know that the alternative model, feeding of the lobes by jets emanating from the nucleus (Blandford & Rees 1974), is the correct one.

Perhaps because of these somewhat inauspicious connections with failed AGN models there has not been a great deal of follow-up work in this area. To our knowledge, the only study of the formation of wakes behind runaway SMBHs in a modern context is de la Fuente Marcos & de la Fuente Marcos (2008), who analyze the gravitational effect of the passage of a SMBH using the impulse approximation. They find that the SMBH can impart a velocity of a few to several tens of km s^{-1} on nearby gas clouds, and that the gas can then become unstable to fragmentation and star formation. The outcome is qualitatively similar to the analysis of Saslaw & De Young (1972), in the sense that, under the right conditions, star formation can occur along the path of the SMBH.

In this paper we report on the serendipitous discovery of a remarkable linear feature in HST images that we suggest may represent such a SMBH-induced wake. We also identify two candidate hyper-compact stellar systems, one embedded in the tip of the wake and the other on the opposite side of the galaxy from which they may have escaped.

2. A 62 KPC LONG LINEAR FEATURE AT $Z = 0.964$

2.1. *Identification in HST/ACS images*

We serendipitously identified a thin, linear feature in *HST* ACS images of the nearby dwarf galaxy RCP 28 (Román et al. 2021; van Dokkum et al. 2022a), as shown in Fig. 1. RCP 28 was observed September 5 2022 for one orbit in F606W and one orbit in F814W, in the context of mid-cycle program GO-16912. The individual `flc` files were combined using `DrizzlePac` after applying a flat field correction to account for drifts in the sensitivity of the ACS CCDs (see van Dokkum et al. 2022b). Upon reducing the data an almost-straight thin streak was readily apparent in a visual assessment of the data quality (see Fig. 1). Based on its appearance we initially thought that it was a poorly-removed cosmic ray, but the presence of the feature in both filters quickly ruled out that explanation. The total AB magnitude of the streak is F814W = 22.87 ± 0.10 and its luminosity-weighted mean color is F606W − F814W = 0.83 ± 0.05.

The streak points to the center of a somewhat irregular-looking galaxy, at $\alpha = 2^{\rm h}41^{\rm m}45\overset{\rm s}{.}43$; $\delta = -8^\circ 20' 55\overset{\prime\prime}{.}4$ (J2000). The galaxy has F814W = 21.86 ± 0.10 and F606W − F814W = 0.84 ± 0.05; that is, the brightness of the streak is $\approx 40\,\%$ of the brightness of the galaxy and both objects have the same color within the errors. Not having encountered something quite like this before in our own images or in the literature, we decided to include the feature in the observing plan for a scheduled Keck run.

2.2. *Redshift*

The feature was observed with the Low-Resolution Imaging Spectrometer (LRIS; Oke et al. 1995) on the Keck I telescope on October 1 2022. The 300 lines mm^{-1} grism blazed at 5000 Å was used on the blue side and the 400 lines mm^{-1} grating blazed at 8500 Å on the red side, with the 680 nm dichroic. The $1\overset{\prime\prime}{.}0$ longslit was used, centered on the galaxy coordinates with a position angle of 327°. The total exposure time was 1800 s, split in two exposures of 900 s. Conditions were good and the seeing was $\approx 0\overset{\prime\prime}{.}8$. On October 3 we obtained a high resolution spectrum with the 1200 lines mm^{-1} grating blazed at 9000 Å in the red. Five exposures were obtained for a total exposure time of 2665 s. Conditions were highly variable, with fog and clouds hampering the observations.

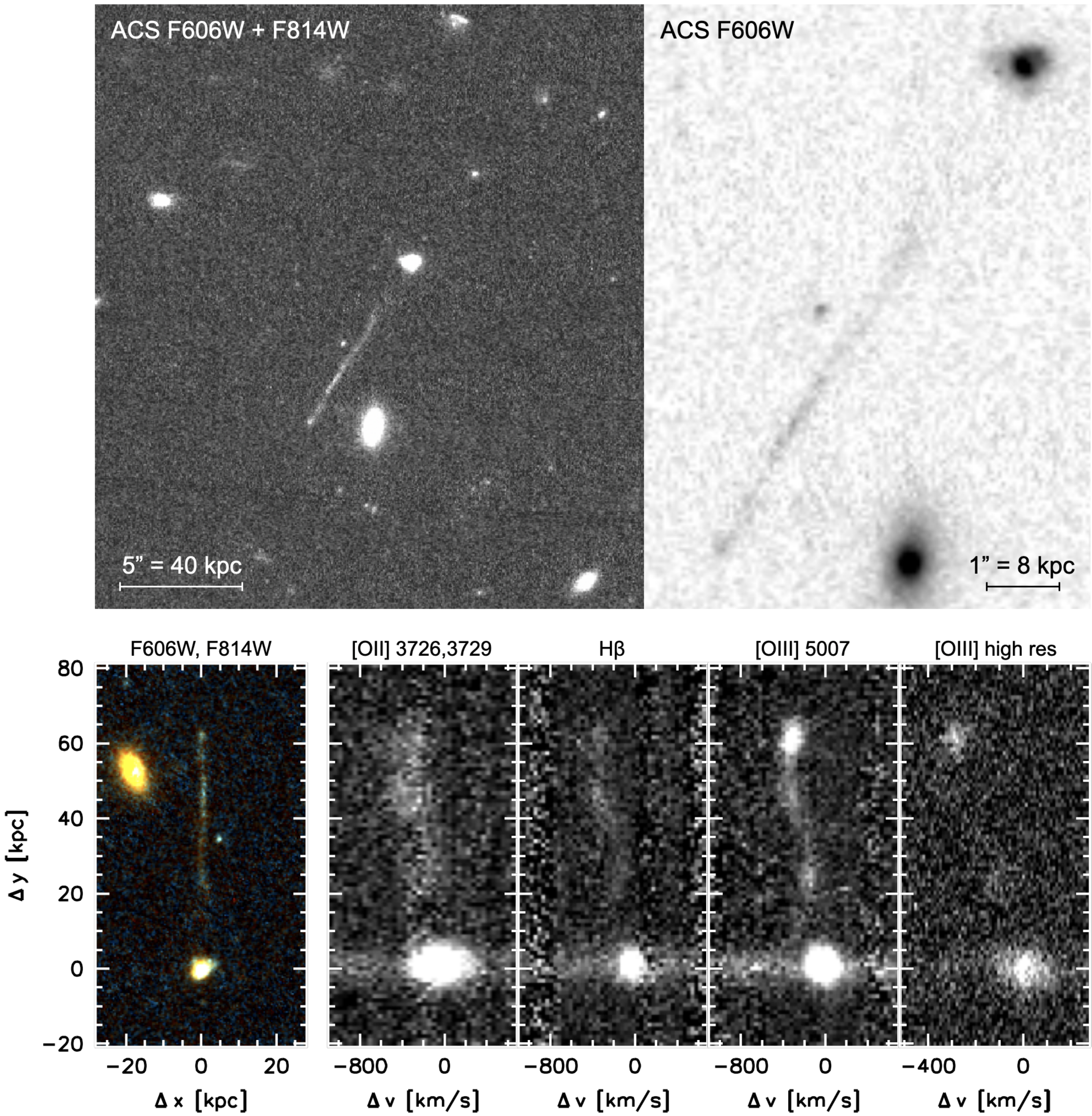

Figure 1. *Top left:* F606W + F814W HST/ACS image of the linear feature and its surroundings. *Top right:* Zoomed view of the F606W image. The feature shows a compact bright spot at the narrow tip, and seems to broaden toward the galaxy. *Bottom left:* Color image, generated from the F606W and F814W images. *Bottom right panels:* Sections of LRIS spectra near bright emission lines. The feature and the galaxy are at the same redshift. The kinematics and line strengths show complex variations along the feature.

Data reduction followed standard procedures for long slit observations. Sky subtraction and initial wavelength calibration were done with the `PypeIt` package (Prochaska et al. 2020). The wavelength calibration was tweaked using sky emission lines, and the data from the individual exposures were combined. A noise model was created and cosmic rays were identified as extreme positive deviations from the expected noise. For the low resolution spectrum a relative flux calibration, enabling the measurement of line ratios, was performed using the spectrophotometric standard HS 2027.

We find continuum and strong emission lines associated with the feature. The lines are readily identified as the redshifted [O II] $\lambda\lambda 3726, 3729$ doublet, Hγ, Hβ, and [O III] $\lambda\lambda 4959, 5007$. The redshift is $z = 0.964$, and the implied physical extent of the feature, from the nucleus of the galaxy to its tip, is 62 kpc. The 2D spectrum in the regions around the strongest emission lines is shown in the bottom panels of Fig. 1. The lines can be traced along the entire length of the feature. There are strong variations in the line strengths and line ratios, as well as in the line-of-sight velocity. We will return to this in following sections. The S/N ratio in the high resolution spectrum is low, about 1/4 of that in the low resolution spectrum.

3. PROPERTIES OF THE HOST GALAXY

3.1. *Morphology*

The same emission lines are detected in the galaxy, confirming that it is at the same redshift as the linear feature (see Fig. 1). The galaxy is compact and somewhat irregular, as shown in Fig. 1 and by the contours in Fig. 2. We determine the half-light radius of the galaxy with `galfit` (Peng et al. 2002), fitting a 2D Sersic profile and using a star in the image to model the point spread function. We find $r_e \approx 1.2$ kpc, but we caution that the fit has significant residuals. The irregular morphology may be due to a recent merger or accretion event, although deeper data are needed to confirm this.

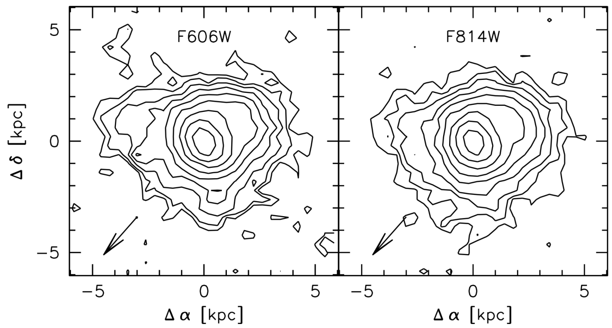

Figure 2. Morphology of the galaxy in F606W and F814W. The arrow indicates the direction of the linear feature. The galaxy is compact, with a half-light radius of $r_e = 1.2$ kpc, and shows irregular features possibly indicating a recent merger and/or a connection to the linear feature.

3.2. *Ionization mechanism*

We measure the strength of the strongest emission lines from the 2D spectra. The continuum was subtracted by fitting a first-order polynomial in the wavelength direction at all spatial positions, masking the lines and their immediate vicinity. Line fluxes were measured by doing aperture photometry on the residual spectra. No corrections for slit losses or underlying absorption are applied. We find an [O III] flux of $F = (10 \pm 1) \times 10^{-17}$ ergs s^{-1} cm^{-2} and [O III]/H$\beta = 1.9 \pm 0.2$.

The interpretation of the line fluxes depends on the ionization mechanism, which can be determined from the combination of [O III]/Hβ and [N II]/Hα. Hα and [N II] are redshifted into the J band, and we observed the galaxy with the Near-Infrared Echellette Spectrometer (NIRES) on Keck II on October 4 2022 to measure these lines. NIRES provides cross-dispersed near-IR spectra from 0.94 μm – 2.45 μm through a fixed $0.''55 \times 18''$ slit. A single 450 s exposure was obtained in good conditions, as well as two adjacent empty field exposures. In the data reduction, the empty field exposures were used for sky subtraction and sky lines were used for wavelength calibration. The Hα and [N II] $\lambda 6583$ emission lines of the galaxy are clearly detected, as shown in the inset of Fig. 3. The emission lines of the galaxy are modeled with the redshift, the Hα line strength, the [N II] line strength, and the velocity dispersion as free parameters. The best-fitting model is shown in red in Fig. 3. We find a velocity dispersion of $\sigma_{\rm gal} = 60 \pm 7$ km s^{-1} and [N II]/H$\alpha = 0.23 \pm 0.06$, with the uncertainties determined from bootstrapping. The implied metallicity, using the Curti et al. (2017) calibration, is $Z = -0.08^{+0.05}_{-0.07}$.

The location of the galaxy in the BPT diagram (Baldwin et al. 1981) is shown in Fig. 3. For reference, data from the Sloan Digital Sky Survey (SDSS) DR7 are shown in grey (Brinchmann et al. 2004). The galaxy is slightly offset from the SDSS relation of star-forming galaxies and quite far from the AGN region in the upper right of the diagram. The offset is consistent with the known changes in the ISM conditions of star forming galaxies with redshift (see, e.g., Steidel et al. 2014; Shapley et al. 2015). The lines in Fig. 3 show the redshift-dependent Kewley et al. (2013) division beyond which AGN begin to contribute to the line ratios. The galaxy is well within the "pure" star formation region for $z = 1$.

3.3. *Star formation rate and stellar mass*

We infer the star formation rate of the galaxy from the Hβ luminosity, which is $L_{\rm H\beta} = (2.5 \pm 0.5) \times 10^{41}$ ergs s^{-1}. The Kennicutt (1998) relation implies an approximate star formation rate of 6 M$_\odot$ yr^{-1} for the dust-free case and 14 M$_\odot$ yr^{-1} for 1 mag of extinction. The stellar mass of the galaxy can be estimated from its luminosity and color. We generate predicted F606W – F814W colors for stellar populations at

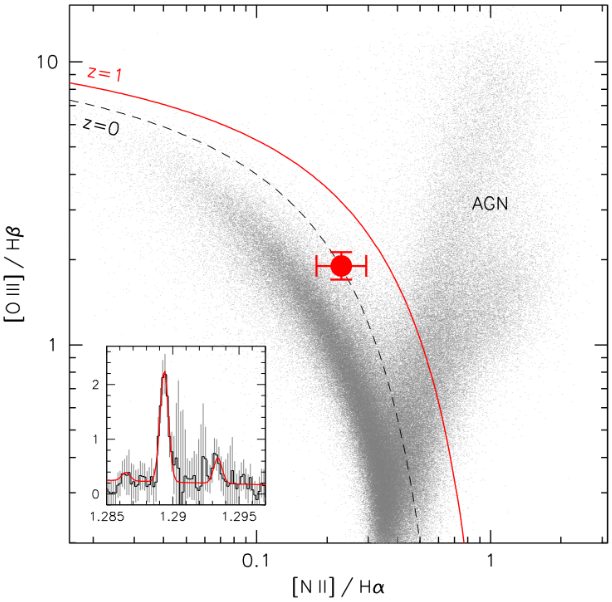

Figure 3. The location of the galaxy in the BPT diagram, with SDSS galaxies in light grey. The lines divide "pure" star forming galaxies from those with an AGN contribution to their line ratios, for $z = 0$ and $z = 1$ (Kewley et al. 2013). The location is as expected for a $z = 1$ star forming galaxy. The inset shows the NIRES spectrum in the Hα region. The red line is the best fit.

$z = 0.964$ with the `Python-FSPS` stellar population modeling suite (Conroy et al. 2009). We find that the observed color of the galaxy can be reproduced with a luminosity-weighted age of ~ 150 Myr and no dust or an age of ~ 65 Myr with $A_V \sim 1$. The implied stellar mass is $M_{\rm gal} \sim 7\times10^9\,{\rm M}_\odot$. The typical star formation rate of a galaxy of this mass at $z = 1$ is $\approx 8\,{\rm M}_\odot\,{\rm yr}^{-1}$ (Whitaker et al. 2014), similar to the observed star formation rate.

We conclude that the galaxy has normal line ratios and a normal specific star formation rate for its redshift. Its age is highly uncertain given that the color is dominated by the most recent star formation, but if we take the $\sim$ 100 Myr at face value, the past-average star formation rate is $\sim 70\,{\rm M}_\odot\,{\rm yr}^{-1}$, an order of magnitude larger than the current value. The galaxy shows morphological irregularities and is overall quite compact. Its half-light radius of 1.2 kpc is a factor of ~ 3 smaller than typical galaxies of its stellar mass and redshift (van der Wel et al. 2014), which implies that its star formation rate surface density is an order of magnitude higher. Taken together, these results suggest that the galaxy experienced a recent merger or accretion event that led to the funneling of gas into the center and a burst of star formation $\sim 10^8$ yr ago.

4. SHOCKS AND STAR FORMATION ALONG THE FEATURE

4.1. *Variation in continuum emission and line ratios*

The linear feature is not uniform in either continuum brightness, color, line strengths, or line ratios. The variation along the feature in the F606W ($\lambda_{\rm rest} = 0.31\,\mu$m) continuum, the F606W − F814W color, and in the [O III] and Hβ lines is shown in Fig. 4. Note that the spatial resolution of the continuum emission is $\sim 8\times$ higher than that of the line emission.

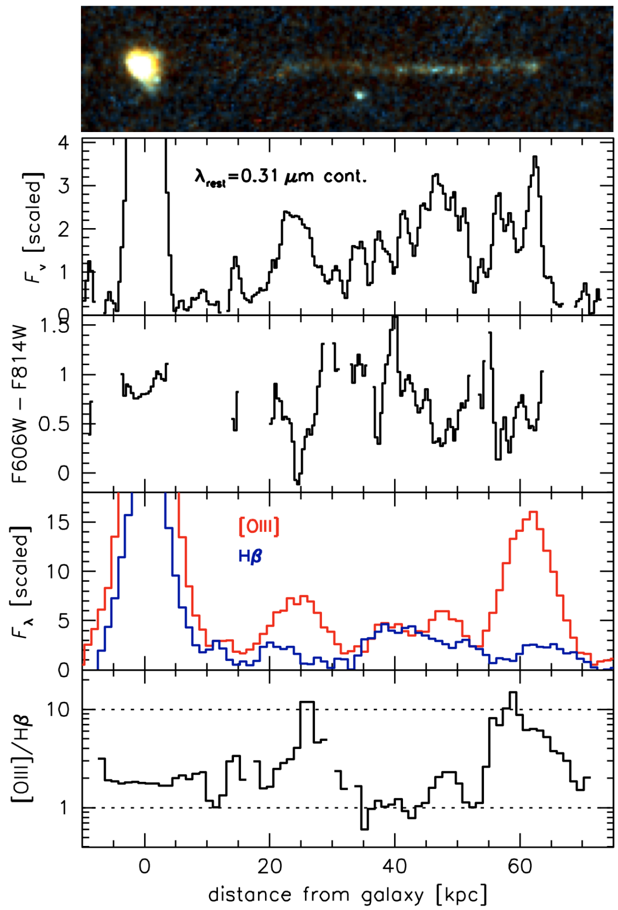

Figure 4. The four panels correspond to the rest-frame near-UV continuum, F606W − F814W color, [O III], and Hβ emission along the linear feature (pictured at the top). The F606W continuum shows strong variation on all spatial scales, and is brightest at the furthest point from the galaxy. The color shows large and seemingly random variations. The [O III]/Hβ ratio varies by a factor of ~ 10 along the feature, with some regions likely dominated by shock ionization and others dominated by H II regions.

There is a general trend of the continuum emission becoming brighter with increasing distance from the galaxy. The continuum reaches its peak in a compact knot at the tip; beyond that point the emission abruptly stops. As shown in Fig. 1 the continuum knot at the tip coincides with a luminous [O III] knot in the spectrum. The [O III] λ5007 flux of the knot is $F \approx 3.9\times10^{-17}$ ergs s^{-1} cm^{-2}, and the luminosity is $L \approx 1.9\times10^{41}$ ergs s^{-1}. The [O III]/Hβ ratio reaches

~ 10 just behind the knot, higher than can be explained by photoionization in H II regions.

The ionization source could be an AGN, although as discussed in more detail in § 6.4.3 the [O III] emission is so bright that an accompanying X-ray detection might be expected in existing Chandra data. An alternative interpretation is that the bright [O III] knot is caused by a strong shock (see Shull & McKee 1979; Dopita & Sutherland 1995; Allen et al. 2008). In the models of Allen et al. (2008), photoionization ahead of a fast ($\gtrsim 500\,\mathrm{km\,s^{-1}}$) shock is capable of producing [O III]/H$\beta \sim 10$, and the expected associated soft X-ray emission (Dopita & Sutherland 1996; Wilson & Raymond 1999) may be below current detection limits. There is at least one more region with elevated [O III]/Hβ ratios (at $r \approx 25$ kpc), and the [O III] emission near the tip could simply be the strongest of a series of fast shocks along the length of the feature.

4.2. *Stellar populations*

In between the two main shocks is a region where O stars are probably the dominant source of ionization. At distances of $40\,\mathrm{kpc} < r < 50\,\mathrm{kpc}$ from the galaxy the [O III]/Hβ ratio is in the $1-2$ range and there are several bright continuum knots. These knots show strong F606W−F814W color variation, mirroring the striking overall variation along the feature that was seen in Fig. 4. In Fig. 5 we compare the measured colors of three knots to predictions of stellar population synthesis models. They were chosen because they span most of the observed color range along the feature. The models span a metallicity range of $-1 \leq Z \leq 0$ and have either no dust (blue) or $A_V = 1$ mag (red). The metallicity range encompasses that of the galaxy ($Z \approx -0.1$).

We find that the knots can indeed be young enough ($\lesssim 10$ Myr) to produce ionizing radiation. However, it is difficult to derive any quantitative constraints as there is no straightforward relation between age and color in this regime. The reason for the complex model behavior in Fig. 5 is that the ratio of red to blue supergiants changes rapidly at very young ages ("blue loops"; see, e.g., Walmswell et al. 2015). We note that the evolution of supergiants is uncertain (see, e.g., Chun et al. 2018) and while the overall trends in the models are likely correct, the detailed behavior at specific ages should be interpreted with caution (see, e.g., Levesque et al. 2005; Choi et al. 2016; Eldridge et al. 2017). In § 7.1 we interpret the overall trend of the color with position along the feature in the context of our proposed model for the entire system.

Finally, we note that the knots appear to have a characteristic separation, as can be seen in Fig. 5 and in the pattern of peaks and valleys from $r = 30$ kpc to $r = 50$ kpc in the F606W emission in Fig. 4. The separation is ≈ 4 kpc. This could be coincidence or be an imprint of a periodicity in the cooling cascade of the shocks.

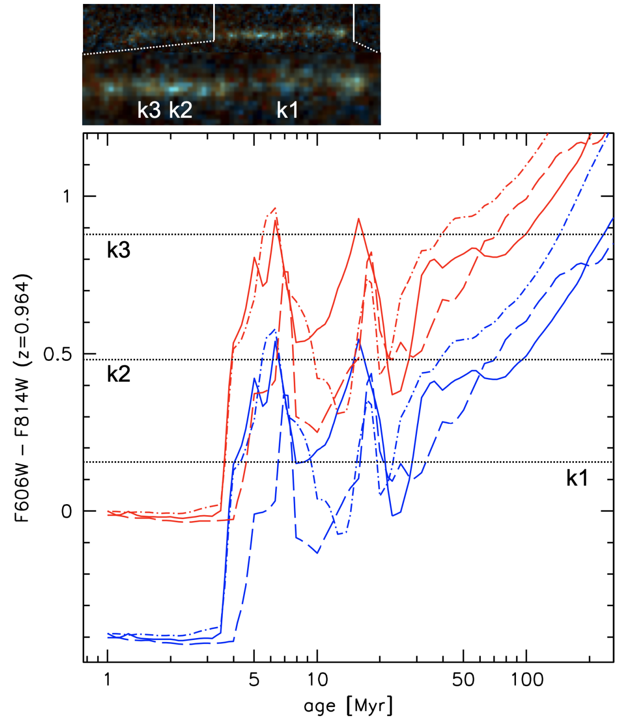

Figure 5. Comparison of the observed colors of several knots in the feature (shown at the top) to model predictions of Conroy et al. (2009) for different ages. Dashed model predictions are for a metallicty $Z = -1$, solid for $Z = -0.5$, and dot-dashed lines are for $Z = 0$. Blue lines are dust-free models and red lines illustrate the effect of dust attenuation with $A_V = 1$. Horizontal lines are measurements for the three knots. The ages of the youngest stars are likely $\lesssim 30$ Myr, but there is no straightforward relation between age and color in this regime. The observed colors span a similar range as the models and are consistent with a wide range of possible metallicities, ages, and dust content.

5. A "COUNTER" LINEAR FEATURE ON THE OTHER SIDE OF THE GALAXY

The LRIS slit covered the galaxy and the feature and also extended beyond the galaxy on the other side. There is no spatially-extended F606W or F814W emission on this side but there is an unresolved object, "B", that is located at a distance of 4.″4 from the galaxy within a few degrees of the orientation of the feature (see Fig. 6). The LRIS spectrum in the vicinity of the redshifted [O III] line is shown in the middle panel of Fig. 6, after subtracting the continuum and dividing by a noise model to reduce the visual effect of sky residuals.

We detect a knot of [O III] λ5007 emission near the location of B, redshifted by $\approx 40\,\mathrm{km\,s^{-1}}$ with respect to the galaxy. Furthermore, there is evidence for faint [O III] emission in between the galaxy and B. This "counter" linear feature is also seen in a u-band image, shown in the right panel of Fig. 6. The object was serendipitously observed with

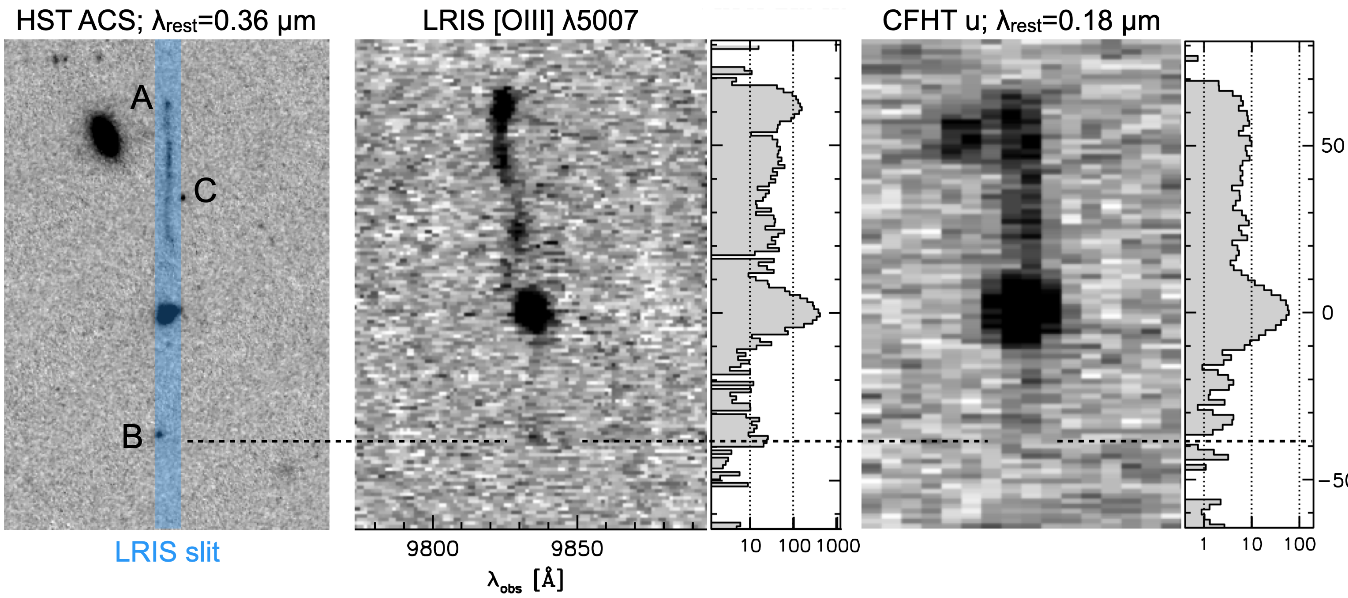

Figure 6. *Left:* Section of the summed ACS F606W+F814W image, with the LRIS slit indicated in blue. Besides the tip of the linear feature, A, there are two other bright spots in the vicinity, B and C. Object B falls in the slit. *Center:* Section of the LRIS spectrum around the [O III] λ5007 line. Object B is detected, as well as faint emission in between B and the galaxy. The attached panel shows the intensity along the feature, on a logarithmic scale. Right: The presence of a "counter" feature is confirmed through its detection in the *u*-band, which samples the rest-frame far-UV. For clarity the *u*-band image was binned by a factor of 6 in the direction perpendicular to the slit (and then expanded again to retain the correct spatial scale). Also note that the primary feature extends all the way to the galaxy, in marked contrast to the pronounced gap between the galaxy and the feature in the ACS image.

MegaPrime on the Canada France Hawaii Telescope (CFHT) on September 11 and 12, 2020 in the context of program 20BO44 (PI: A. Ferguson). The total exposure time was 11,880 s; the data reduction is described in M. L. Buzzo et al., in preparation.

The *u*-band surface brightness of the counter feature is approximately $5\times$ fainter than on the other side, and it appears to terminate at the location of the [O III] knot. Furthermore, the primary feature extends all the way to the galaxy in the *u*-band: there is no gap at $r \lesssim 25$ kpc as is the case in the ACS data. The *u*-band samples the rest-frame far-UV ($\lambda_{\rm rest} \approx 0.18\,\mu$m), and we conclude that the far-UV emission of the entire system is largely decoupled from the near-UV emission that is sampled with ACS. The total far-UV brightness of the linear emission is ≈ 70 % of the far-UV brightness of the galaxy, whereas this fraction is only ≈ 40 % at $\lambda_{\rm rest} \approx 0.36\,\mu$m.

The detection of the counter feature in the rest-frame far-UV shows that the [O III] emission is likely real and caused by shocks. The combination of [O III] line emission and far-UV continuum emission has been linked to cooling radiation of fast ($\gtrsim 100$ km s^{-1}) shocks, both theoretically (e.g., Sutherland et al. 1993), and observationally, for instance in sections of supernova remnants (Fesen et al. 2021).

It is difficult to determine the relationship between object B and the counter feature. It has F814W = 25.28 ± 0.10 (AB) and F606W − F814W = 0.84 ± 0.14, and it is misaligned by 4° from the line through A and the galaxy. We will discuss the nature of B in the context of our preferred overall model for the system in § 6.4. There is also another compact object, C, that is nearly exactly opposite to B in angle and distance. This object was not covered by the LRIS slit and we have no information about it, except that it is bluer than B.

6. INTERPRETATION

6.1. *Various straight-line extragalactic objects*

With the basic observational results in hand we can consider possible explanations. Thin, straight optical features that extend over several tens of kpc have been seen before in a variety of contexts. These include straight arcs, such as the one in Abell 2390 (Pello et al. 1991); one-sided tidal tails, with the Tadpole galaxy (Arp 188) being the prototype (Tran et al. 2003); debris from disrupted dwarf galaxies, like the multiple linear features associated with NGC 1097 (Amorisco et al. 2015); ram pressure stripped gas, such as the spectacular 60 kpc $\times$ 1.5 kpc Hα feature associated with the Coma galaxy D100 (Cramer et al. 2019); and "superthin" edge-on galaxies (Matthews et al. 1999).

A gravitational lensing origin is ruled out by the identical redshift of the galaxy that the feature points to. Tidal effects, ram pressure stripping, or a superthin galaxy might explain aspects of the main linear feature but are not consistent with the shocked gas and lack of rest-frame optical continuum emission on the other side of the compact galaxy.

Given the linearity of the entire system, the symmetry with respect to the nucleus, the presence of shocked gas without continuum emission, as well as the brightness of both the entire feature and the [O III] emission at the tip, the most viable explanations all involve SMBHs – either through nuclear activity or the local action of a set of runaway SMBHs.

6.2. *An optical jet?*

Visually, the closest analog to the linear feature is the famous optical jet of the $z = 0.16$ quasar 3C 273 (Oke & Schmidt 1963; Bahcall et al. 1995): its physical size is in the same regime (about half that of our object) and it has a similar axis ratio and knotty appearance. However, the detection of bright emission lines along the feature is strong evidence against this interpretation. The spectra of jets are power laws, and there are no optical emission lines associated with optical jets or hot spots (Keel & Martini 1995).

Furthermore, the 3C 273 jet and 3C 273 itself are very bright in the radio and X-rays, with different parts of the jet showing low- and high-energy emission (see Uchiyama et al. 2006). We inspected the VLA Sky Survey (VLASS; Lacy et al. 2020) as well as a 60 ks deep Chandra image[1] of the field that was obtained in 2005 in the context of program 5910 (PI Irwin). There is no evidence for a detection of the linear feature or the galaxy, with either the VLA or Chandra. We note that the $z = 0.96$ feature might be expected to have an even higher X-ray luminosity than 3C 273 if it were a jet, as the contribution from Compton-scattered CMB photons increases at higher redshifts (see Sambruna et al. 2002).

6.3. *Jet-induced star formation?*

Rather than seeing direct emission from a jet, we may be observing jet-induced star formation (Rees 1989; Silk 2013). There are two well-studied nearby examples of jets triggering star formation, Minkowski's object (Croft et al. 2006) and an area near a radio lobe of Centaurus A (Mould et al. 2000; Crockett et al. 2012). There are also several likely cases in the more distant Universe (Bicknell et al. 2000; Salomé et al. 2015; Zovaro et al. 2019). The overall idea is that the jet shocks the gas, and if the gas is close to the Jeans limit subsequent cooling can lead to gravitational collapse and star formation (see, e.g., Fragile et al. 2017). The presence of both shocks and star formation along the feature is qualitatively consistent with these arguments (see Rees 1989).

The most obvious problem with this explanation is that there is no evidence for nuclear activity in our object from the BPT diagram, the VLASS, or Chandra imaging (see above). It is possible, however, that the AGN turned off between triggering star formation and the epoch of observation, qualitatively similar to what is seen in Hanny's Voorwerp and similar objects (Lintott et al. 2009; Keel et al. 2012; Smith et al. 2022).

A more serious issue is that the morphology of the feature does not match simulations or observations of jet-induced star formation. First, as can be seen most clearly in the top right panel of Fig. 1, the feature is narrowest at the tip rather than the base. By contrast, for a constant opening angle a jet linearly increases its diameter going outward from the host galaxy, reaching its greatest width at the furthest point (as illustrated by HST images of the M87 jet, for instance; Biretta et al. 1999). Second, the interaction is most effective when the density of the jet is lower than that of the gas, and the shock that is caused by the jet-cloud interaction then propagates largely *perpendicular* to the jet direction (e.g., Ishibashi & Fabian 2012; Silk 2013; Fragile et al. 2017). This leads to star formation in a broad cocoon rather than in the radial direction, as shown explicitly in the numerical simulations of Gaibler et al. (2012). It is possible for the jet to subsequently break out, but generically jet-cloud interactions that are able to trigger star formation will decollimate the jet.

A related problem is that the observed velocity dispersion of the shocked gas is low. From the high resolution LRIS spectrum we find a velocity dispersion of $\lesssim 20\,\mathrm{km\,s^{-1}}$ in the main shock at the tip of the feature, which can be compared to $\sigma \sim 130\,\mathrm{km\,s^{-1}}$ in the shocked gas of Centaurus A (Graham 1998) and $\sigma \sim 50\,\mathrm{km\,s^{-1}}$ predicted in recent simulations (Mandal et al. 2021). Most fundamentally, though, the feature is the inverse of what is expected: the strongest interactions should not be at the furthest point from the galaxy but close-in where the ambient gas has the highest density, and the feature should not become more collimated with distance but (much) less.

6.4. *Runaway supermassive black holes*

This brings us to our preferred explanation, the wake of a runaway SMBH. The central argument is the clear narrow tip of the linear feature, which marks both the brightest optical knot and the location of very bright [O III] emission, combined with the apparent fanning out of material behind it (as can be seen in the top right panel of Fig. 1). As discussed below (§ 6.4.2) this scenario can accommodate the feature on the other side of the galaxy, as the wake of an escaped binary SMBH resulting from a three body interaction. The properties of the (former) host galaxy can also be explained. Its compactness and irregular isophotes are evidence of the gas-rich recent merger that brought the black holes together, and the apparent absence of an AGN reflects the departure of all SMBHs from the nucleus.

6.4.1. *Mechanisms for producing the linear feature*

As discussed in § 1 there have not been many studies of the interaction of a runaway SMBH with the circumgalactic gas, and there is no widely agreed-upon description of

[1] https://doi.org/10.25574/05910

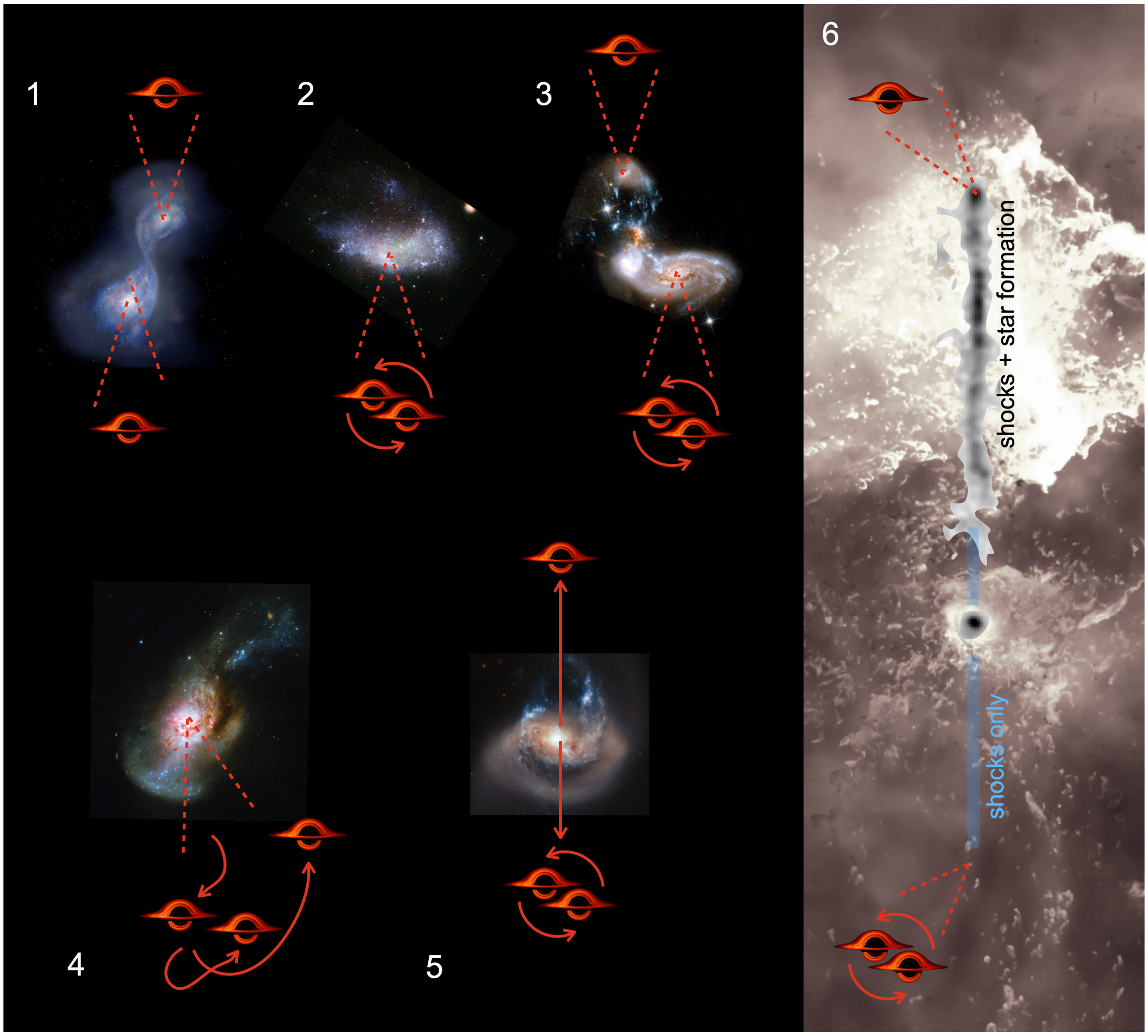

Figure 7. Schematic illustration of the runaway SMBH scenario as an explanation of the key observed features. Panels 1–5 show a "classical" slingshot scenario (e.g., Saslaw et al. 1974). First, a merger leads to the formation of a long-lived binary SMBH (1,2). Then a third galaxy comes in (3), its SMBH sinks to the center of the new merger remnant, and this leads to a three-body interaction (4). One black hole (usually the lightest) becomes unbound from the other two and receives a large velocity kick. Conservation of linear momentum implies that the remaining binary gets a smaller velocity kick in the opposite direction. If the kicks are large enough all SMBHs can leave the galaxy (5). There can be $\gtrsim 1$ Gyr between the events in panels (2) and (3). Panels (4) and (5) happened ~ 40 Myr before the epoch of observation. The background of (6) is a frame from an Illustris TNG simulation (Pillepich et al. 2018), with lighter regions having higher gas density. This illustrates that there can be highly asymmetric flows in the circumgalactic medium, and we speculate that the SMBH at A is traveling through such a region of relatively dense and cold CGM (see text).

what is expected to happen. Saslaw & De Young (1972) focus on the direct interaction between gas that is associated with the SMBH with the ambient gas. They predict a strong bow shock which moves supersonically with the SMBH through the gas. The aftermath of the shock leads to a cooling cascade, ultimately leading to star formation in a wake behind the SMBH. de la Fuente Marcos & de la Fuente Marcos (2008) study the gravitational effect of the passage of a SMBH on the ambient gas. They find that small velocity kicks, of up to several tens of km s^{-1}, are imparted on the gas, and that the subsequent new equilibrium can lead to gravitational collapse and star formation. There can be a delay between the passage of the SMBH and the triggering of star formation, depending on the impact parameter and the properties of the clouds.

Both mechanisms may be important; we certainly see evidence for both star formation and shocks along the wake, including potentially a bow shock at or just behind the location of the SMBH itself, and conclude that the observations are at least qualitatively consistent with the models that exist. It is important to note that in these models the star formation does not take place in gas that was previously bound to the SMBH, but in the circumgalactic medium. The kinematics and metallicity of the gas therefore largely reflect its pre-existing state, perhaps slightly modified by the passage of the SMBH.

6.4.2. *Nature of the counter wake*

In this scenario there is only one explanation for the counter feature on the other side of the galaxy, namely shocked gas in the wake of a second runaway SMBH. This is not as far-fetched as it may seem. When a third SMBH arrives in the vicinity of a pre-existing binary SMBH, a common outcome of the three body interaction is that one SMBH becomes unbound from the other two. The post-interaction binary can be the original one or contain the new arrival (Saslaw et al. 1974). In either case both the unbound SMBH and the binary get a kick, in opposite directions and with the velocity inversely proportional to the mass (Saslaw et al. 1974; Rees & Saslaw 1975). The counter feature is then the wake of the most massive product of the three body interaction, namely the binary SMBH.

The relative projected length of the wakes is 62 kpc / 36 kpc = 1.7:1. Here we used the location of object B to determine the length of the counter wake; using the location of the [O III] knot instead gives the same ratio. Although modified by their climb out of the potential well, this length ratio is likely not far from the velocity ratio of the black holes, at least if $v_{\rm BH} \gg v_{\rm esc}$. Generally the least massive object is expected to escape (i.e., become unbound) from the other two in a three-body interaction, with the escape probability $\propto M_{\rm BH}^{-3}$ (Valtonen & Mikkola 1991). As the escaped SMBH has a lower mass than each of the two components of the binary, the velocity ratio between the single SMBH and the binary SMBH is then always $> 2:1$, if linear momentum is conserved. A lower velocity ratio can work but only if the three SMBHs all have similar masses, for instance 4:4:3 for a:b1:b2, with b1 and b2 the two components of the binary. In a 4:4:3 three body interaction the probability that either one of the most massive objects escapes (leading to the observed 1.7:1 ratio) is about the same as the probability that the least massive one escapes.

We note that simulations indicate that complete ejections of all SMBHs from the halo are expected to be rare, occurring only in $\sim 1\,\%$ of three-body interactions (Hoffman & Loeb 2007). The dynamics are complex, however, particularly when black hole spin, gravitational wave radiation, and gas flows into the center are taken into account (see, e.g., Escala et al. 2005; Iwasawa et al. 2006; Chitan et al. 2022). Along these lines, a modification of the simple slingshot is that the binary hardens due to the interaction with the third SMBH and merges, leading to a gravitational recoil kick. This could explain how the binary made it so far out of the galaxy, without the need for the three SMBHs to have near-equal masses. However, the direction and amplitude of the recoil depends on the mass ratios, spins, and relative orientation of the binary at the time of the merger (e.g., Herrmann et al. 2007; Lousto & Zlochower 2011), and it seems unlikely that the two wakes would be exactly opposite to one another in this scenario.

The counter wake is not only shorter than the primary wake in the observed *u*-band but also much fainter, which indicates that the shock has a lower velocity. The shock (and black hole) velocities are undetermined – although we will constrain them in the next section – but as noted above, the velocity ratio between the wake and counterwake is likely 1.7. Assuming that the sound speed is similar on both sides of the galaxy, the far-UV luminosity of fast shocks is expected to scale with the velocity of the shock as $L_{\rm UV} \propto v_{\rm shock}^3$ (Dopita & Sutherland 1995). The expected ratio of the UV surface brightness of the two wakes is therefore $1.7^3 = 5$, in excellent agreement with the observed ratio (also 5; see § 5). The post-shock pressure and temperature scale as $\sim v_{\rm shock}^2$, and are therefore a factor of ~ 3 lower in the counter wake. This may explain the lack of gravitational collapse and star formation, although the local conditions of the CGM may also play a role (see § 8).

6.4.3. *Locations of the SMBHs*

The "smoking gun" evidence for this scenario would be the unambiguous identification of the black holes themselves. The approximate expected (total) SMBH mass is $M_{\rm BH} \sim 2 \times 10^7\,{\rm M}_\odot$, for a bulge mass of $7 \times 10^9\,{\rm M}_\odot$ and assuming the relation of Schutte et al. (2019). The obvious places to look for them are A and B in Fig. 6. These are candidates for "hyper compact stellar systems" (Merritt et al. 2009), SMBHs enveloped in stars and gas that escaped with them. The expected sizes of HCSSs are far below the resolution limit of HST and the expected stellar masses are bounded by the SMBH mass, so of order $10^5\,{\rm M}_\odot - 10^7\,{\rm M}_\odot$.

Focusing first on A, the tip of the feature is compact but not a point source: as shown in the detail view of Fig. 5 there are several individual bright pixels with different colors embedded within the tip. The approximate brightness of these individual knots is F814W ≈ 29.5, after subtracting the local background. This corresponds to a stellar mass of $10^6\,{\rm M}_\odot - 10^7\,{\rm M}_\odot$, in the right range for a HCSS.

The complex tip of the feature coincides with very bright [O III] emission, and an interesting question is whether this could be the equivalent of the narrow line region (NLR) of an AGN. If so, it is not composed of gas that is bound to the black hole, as in that case the velocity dispersion would be at least an order of magnitude higher. Instead, it would be a "traveling" NLR, with the accretion disk of the SMBH illuminating the neighboring circumgalactic medium as it moves through it. If the accretion disk produces enough hard UV photons to ionize the local CGM it should also emit X-rays. The empirical relation between [O III] luminosity and X-ray luminosity of Ueda et al. (2015) implies $L_X \sim 3 \times 10^{43}$ ergs s^{-1}, and with standard assumptions this correspond to ~ 40 counts in the existing 60 ks Chandra image. However, no object is detected, and we tentatively conclude that it is unlikely that the SMBH at A is active. This is not definitive and further study is warranted: the Ueda et al. (2015) relation has significant scatter and the object is on the edge of the Chandra pointing, leading to a wide PSF and relatively poor point source sensitivity.

We note that it is possible that the SMBH that is producing the shocks and star formation at location A is not located there, but is further than 62 kpc from the galaxy. In the de la Fuente Marcos & de la Fuente Marcos (2008) picture there is a delay between the gravitational impulse and the onset of star formation of about ~ 30 Myr. For a black hole velocity of $\sim 10^3$ km s^{-1} this means that the SMBH may be several tens of kpc ahead of the feature. A careful inspection of the HST image shows no clear candidates for a HCSS beyond the tip.

Turning now to object B, it is a point source at HST/ACS resolution that is clearly distinct from the shocked gas that constitutes the counter wake. However, at F814W = 25.3 (see § 5) it is uncomfortably bright in the context of expectations for a HCSS. The stellar mass of B is $\sim 3 \times 10^8\,M_\odot$ if the same M/L ratio is assumed as for the galaxy, an order of magnitude higher than the probable black hole mass.

A possible explanation for the brightness of B is that it is a chance superposition of an unrelated object, and that the apparent termination of the counter wake at that location is coincidental. We show a detailed view of the areas around A and B in Fig. 8. The green bands indicate the locations of the [O III] knots on each side of the galaxy, with the width of the band the approximate uncertainty. The [O III] knot at the end of the counter wake appears to be 0.″25 beyond B. Also, the angle between B and the galaxy is 4° offset from the angle between A and the galaxy. There is no obvious candidate HCSS at the expected location (marked by 'X'), but that may be due to the limited depth of the 1+1 orbit ACS data.

Finally, object C is a third candidate HCSS, but only because of its symmetric location with respect to B. In some dynamical configurations it may be possible to split an equal-mass binary, with B and C the two components, or to have multiple binary black holes leading to a triple escape. These scenarios are extremely interesting but also extremely far-fetched, and without further observational evidence we consider it most likely that C is a chance alignment of an unrelated object.

7. MODELING

Here we assume that the runaway SMBH interpretation is correct, and aim to interpret the details of the wake in the HST images in this context. In § 7.1 we fit the seemingly random color variations along the wake and in § 7.2 we link the line-of-sight velocity variation along the wake to spatial variations in the HST image. In both subsections we assume that the SMBH is currently located at position A and that it triggered star formation instantaneously as it moved through the circumgalactic gas.

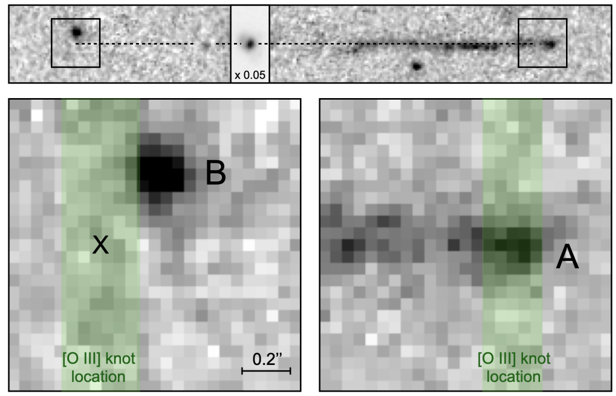

Figure 8. Detailed view of the areas around A and B, in the summed F606W + F814W image. Green bands indicate the locations of [O III] knots in the LRIS spectrum. If B is a chance projection along the line of sight, a hyper compact stellar system may be detectable near the cross in deeper data. In the vicinity of A, the complex interplay of shocks, star formation, and the SMBH itself could be investigated with high resolution IFU spectroscopy.

7.1. *Stellar ages*

The color variation along the wake is shown in Fig. 9. The information is identical to that in Fig. 4, except we now show errorbars as well. Colors were measured after averaging the F606W and F814W images over 0.″45 (9 pixel) in the tangential direction and smoothing the data with a 0.″15 (3 pixel) boxcar filter in the radial direction. This is why some prominent but small-scale features, such as the blue pixel at $r = 42$ kpc, do not show up clearly in the color profile. Data at $r > 58$ kpc are shown in grey as they are assumed to be affected by the SMBH itself (the candidate hyper compact stellar system "A" – see § 6.4.3). Data at $r < 5$ kpc are part of the galaxy and not of the wake.

We fit the single burst stellar population synthesis models of Fig. 5 to the data. The three metallicities shown in Fig. 5, $Z = 0$, $Z = -0.5$, and $Z = -1$, were fit separately. Besides the choice of metallicity there are two free parameters: the overall dust content and the time since the SMBH was ejected $\tau_{\rm eject}$. The age of the stellar population τ' is converted to a position using

$$r' = 62 - 62\frac{\tau'}{\tau_{\rm eject}}. \quad (1)$$

The best-fitting $Z = -0.5$ model has $A_V = 1.1$ and $\tau_{\rm eject} = 39$ Myr, and is shown by the red curve in Fig. 9. The other metallicities gave similar best-fit parameters but much higher

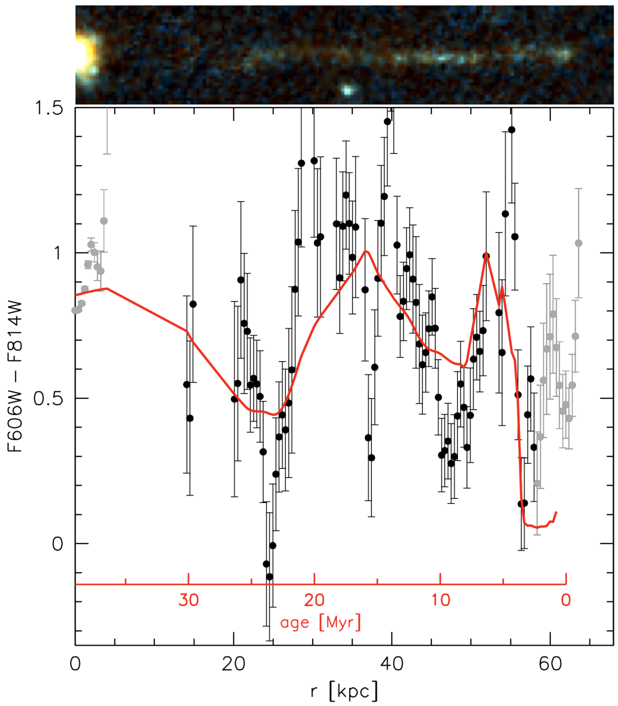

Figure 9. Observed F606W − F814W color along the wake, after smoothing with a 0.″15 boxcar filter. The red curve is a simple stellar population with $Z = -0.5$, $A_V = 1.1$ mag, and age varying linearly with position along the wake. The best-fit time since ejection is 39 Myr, corresponding to a projected black hole velocity of $v_{\rm BH} \approx 1600\,{\rm km\,s^{-1}}$.

χ^2 values. This simple model reproduces the main color variation along the wake, with three cycles going from blue to red colors starting at $r = 56$ kpc all the way to $r = 15$ kpc. As noted earlier, these large and sudden color changes in the model curve reflect the complex evolution of red and blue supergiants, and are *not* due to a complex star formation history. The red axis shows the corresponding age of the stellar population.

The best-fitting $\tau_{\rm eject}$ implies a projected black hole velocity of $v_{\rm BH} \approx 1600\,{\rm km\,s^{-1}}$. This velocity is in the expected range for runaway SMBHs (e.g., Saslaw et al. 1974; Volonteri et al. 2003; Hoffman & Loeb 2007), providing further evidence for this interpretation. Specifically, it is too high for outflows and too low for relativistic jets; besides hypervelocity stars, which are thought to have a similar origin (Hills 1988), runaway SMBHs are the only objects that are likely to have velocities in this range.

7.2. *Kinematics*

The black hole velocity of $\approx 1600\,{\rm km\,s^{-1}}$ that we derive above is much higher than the observed line-of-sight velocities of gas along the wake, which reach a maximum of $\approx 330\,{\rm km\,s^{-1}}$ (see Fig. 1). The observed velocities reflect the kinematics of the circumgalactic medium: the passing black hole triggers star formation in the CGM behind it but does not drag the gas or the newly formed stars along with it.

In this picture the gas and newly formed stars will continue to move after the black hole has passed. The wake should therefore not be perfectly straight but be deflected, reflecting the local kinematics of the CGM. We show the F606W + F814W HST image of the wake in the middle left panel of Fig. 10, with the vertical axis stretched to emphasize deviations from linearity. The wake is indeed not perfectly straight, but shows several "wiggles" with an amplitude of ~ 0.5 kpc. These deviations from a straight line are quantified by fitting a Gaussian to the spatial profile at each position along the wake and recording the centroids. These are indicated with orange dots in the middle left panel and with black points with errorbars in the bottom right panel.

The [O III] λ5007 velocity profile is shown in the top left panel, with the orange line a spline fit to the changing velocity centroids along the wake. The velocity profile shows a pronounced change between 35 kpc and 40 kpc, where the line-of-sight velocity increases from $\approx 150\,{\rm km\,s^{-1}}$ to $\approx 300\,{\rm km\,s^{-1}}$. There is a change at the same location in the spatial profile, suggesting that the deviations from a straight line are indeed correlated with the CGM motions.

We model the connection between the line-of-sight velocities and the wiggles in the HST image in the following way. We assume that the black hole leaves the galaxy in a straight line with velocity $v_{\rm BH}$ and that it triggers star formation instantaneously at each location that it passes. The newly formed stars will move with a velocity $\beta v_{\rm gas}$, where $v_{\rm gas}$ is the line-of-sight velocity measured from the [O III] line and β is a conversion factor between line-of-sight velocity and velocity in the plane of the sky tangential to the wake. By the time that the SMBH reaches 62 kpc, the stars at any location along the wake r will have moved a distance

$$d(r) = \beta v_{\rm gas}(r)\frac{62-r}{v_{\rm BH}} \qquad (2)$$

that is, the velocity in the plane of the sky multiplied by the time that has elapsed since the passage of the black hole.

As $v_{\rm gas}$ is directly measured at all r, the only free parameter in Eq. 2 is $\beta^{-1}v_{\rm BH}$. In practice there are several nuisance parameters: the model can be rotated freely with respect to the center of the galaxy, and there may be an offset between the line-of-sight velocity of the galaxy and that of the CGM at $r = 0$. We use the `emcee` package (Foreman-Mackey et al. 2013) to fit for the black hole velocity and the nuisance parameters. The number of samples is 1200 with 300 walkers; we verified that the fit converged.

The best fit is shown by the red line in the bottom right panel and the bottom left panel of Fig. 10. The fit reproduces the spatial variation quite well, particularly when considering that $v_{\rm gas}$ is measured from data with 8× lower resolution. The posterior distribution of $\beta^{-1}v_{\rm BH}$ is shown in the top

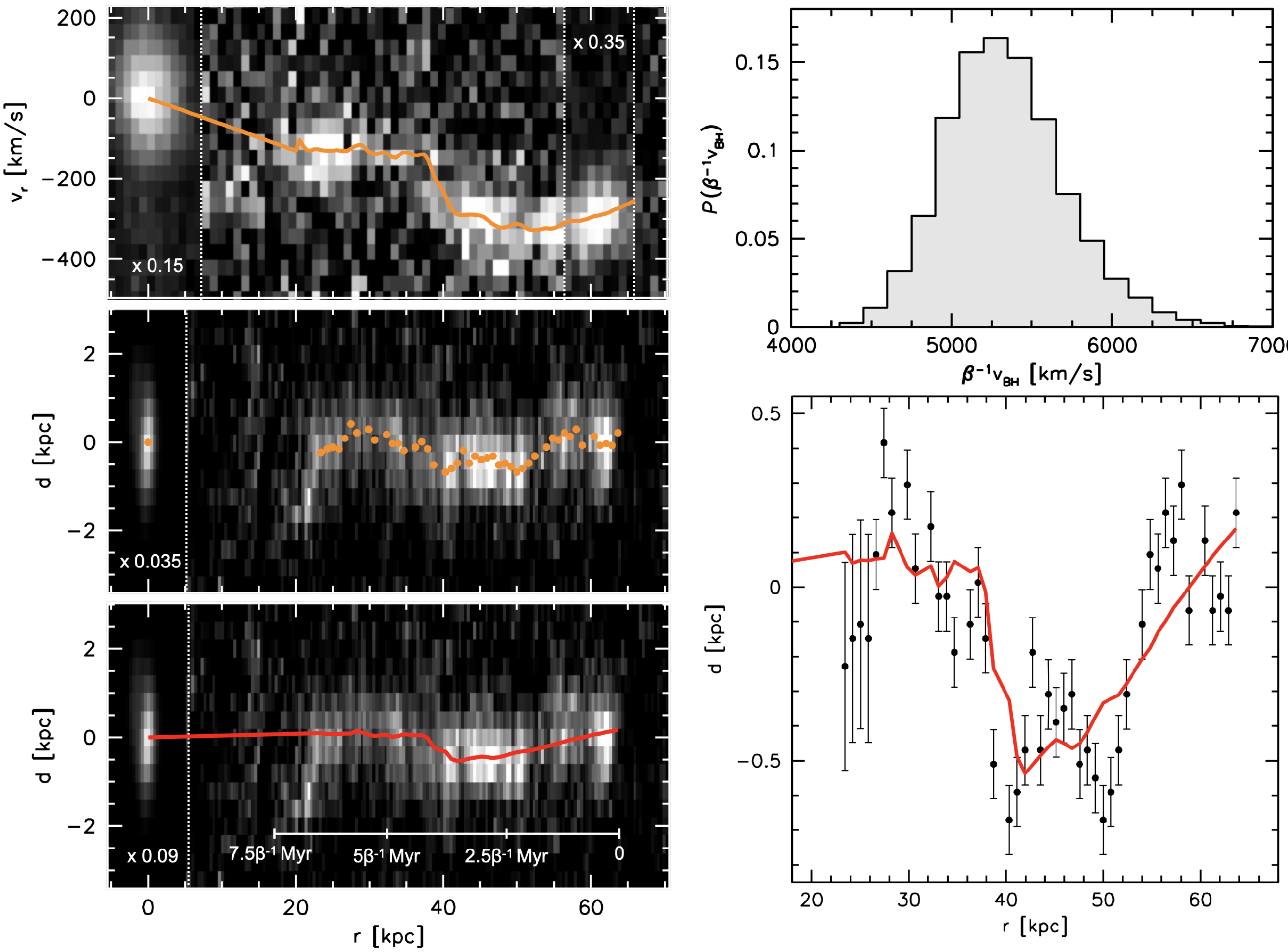

Figure 10. Connection between velocities along the wake and its morphology. *Top left:* [O III] emission along the wake, with a fit to the velocity centroids in orange. *Middle left:* HST image of the wake, with stretched vertical axis to emphasize variations. The orange dots are centroids. *Bottom right:* Fit of a kinematic model to the HST centroids, based on the [O III] velocity profile. This fit is also shown in the bottom left panel. *Upper right:* Distribution of posteriors for the black hole velocity $v_{\rm BH}$, modified by an unconstrained geometric parameter β. For $\beta \approx 0.3$ we find that $v_{\rm BH}$ is consistent with the value derived from the color variation along the wake.

right panel. We find $v_{\rm BH} = \beta 5300^{+400}_{-300}$ km s^{-1}. The constraint comes directly from the amplitude of the wiggles: if the black hole velocity were lower by a factor two, twice as much time would have passed since the passage of the SMBH, and the wake would have drifted apart twice as much (≈ 1 kpc instead of the observed ≈ 0.5 kpc).

Combining this result with that from § 7.1 we infer that the morphological deviations from a straight line and the colors of the wake can be simultaneously explained if $\beta \approx 0.3$, that is, if the gas velocities perpendicular to the wake are 30 % of the line-of-sight velocities. The implied direction of motion is about 17° away from the line of sight (with an unknown component in the plane of the sky along the wake).

8. DISCUSSION AND CONCLUSIONS

In this paper we report the discovery of a remarkable linear feature that is associated with a galaxy at $z = 0.96$. Although the feature exhibits superficial similarities to other thin objects, in particular the optical jet of 3C 273, close examination shows that it is quite unique with no known analogs.

We make the case that the feature is the wake of a runaway SMBH, relying on the small number of papers that have been written on this topic in the past fifty years (Saslaw & De Young 1972; Rees & Saslaw 1975; de la Fuente Marcos & de la Fuente Marcos 2008). This area could benefit from further theoretical work, particularly since these papers propose a variety of formation mechanism for the wakes. Hydrodynamical simulations that model the shocks and also take gravitational effects into account might bring these initial studies together in a self-consistent framework.

Objects A and B are possible hyper compact stellar systems (HCSSs; Merritt et al. 2009). Neither object is a clearcut case: object A is not a point source, and the actual HCSS would be one of several candidates within the main knot. Object B is brighter than what might be expected for a HCSS (see Boylan-Kolchin et al. 2004; Merritt et al. 2009), and as we show in § 6.4.3 it may well be a chance superposition of an unrelated object. It could also be that Merritt et al. (2009) underestimate the mass that can be bound to the black hole (as they do not take the effects of gas or possible binarity of the SMBH into account), that the M/L ratio of B is much lower than what we estimate, or that the SMBH is more massive than what we inferred from the galaxy mass.

We show that the seemingly random color variation along the wake can be explained by a simple model of aging of the stars, beginning at the tip of the wake. In this interpretation the striking excursions in Fig. 9 are due to the varying dominance of blue and red supergiants.[2] The evolution of these stars is quite uncertain; turning the argument around, the data provide a validation of the qualitative behavior of the models from 1 to 30 Myr. The implied velocity of the SMBH at A is $v_{\rm BH} \sim 1600\,{\rm km\,s^{-1}}$ and the velocity of the binary SMBH is $v_{\rm BH} \sim 900\,{\rm km\,s^{-1}}$ if the ejection was symmetric. These velocities are projected on the plane of the sky, and do not correspond to predicted line-of-sight velocities; the ratio between the line-of-sight velocities should be ~ 1.7 but their absolute values are poorly constrained.

Velocities in this range are also indicated by the straightness of the HST feature: as we show in § 7.2 the feature is expected to differentially disperse, and its morphology requires that it was created by a fast-moving object. A third piece of evidence for high speeds comes from the emission line ratios. As noted in § 3.2 it is difficult to have [O III]/Hβ ratios as high as ~ 10 unless there is a significant precursor component (photoionization ahead of the shock) and the shock has a velocity of at least $\sim 500\,{\rm km\,s^{-1}}$ (Allen et al. 2008). We can speculate that the precursor component may be partially responsible for the complexity of the tip of the feature: perhaps star formation is not only triggered behind the SMBH but also just in front of it.

The shock velocity and luminosity provide a constraint on its spatial extent. From Eqs. 3.4 and 4.4 in Dopita & Sutherland (1996) with $L_{\rm H\beta} \sim 2 \times 10^{40}\,{\rm ergs\,s^{-1}}$ and $v_{\rm shock} \sim 1600\,{\rm km\,s^{-1}}$ we obtain an area of the shockfront of $\sim 0.2n^{-1}\,{\rm kpc}^2$, with n the density in cm^3. For $n < 0.1$ (as expected for circumgalactic gas, even with some gravitational compression) the shock should be resolved at HST resolution, and possibly even from the ground. In this context it is interesting that there is some indication that the [O III] emission is indeed resolved along the LRIS slit. Turning this argument around, a high resolution image of the shock (in either [O III] or the rest-frame far-UV) could provide a joint constraint on the shock velocity and the density of the gas.

The measured line-of-sight velocities along the wake do not tell us much about the velocity of the SMBH and its accompanying shocks, but they do provide a pencil beam view of circumgalactic gas kinematics in a regime where we usually have very little information. We can compare the kinematics to general expectations for halo gas. The $z = 1$ stellar mass – halo mass relation implies a halo mass of $\approx 3 \times 10^{11}\,{\rm M_\odot}$ (Girelli et al. 2020) and a virial radius of $\approx 80\,{\rm kpc}$ (Coe 2010). Considering that the projected length of the wake is shorter than the physical length, the $r_{\rm proj} = 62\,{\rm kpc}$ wake likely extends all the way to the virial radius. Using $V_{\rm vir} = (GM_{\rm vir}/r_{\rm vir})^{0.5}$ we have $V_{\rm vir} \approx 130\,{\rm km\,s^{-1}}$, much lower than the observed peak line-of-sight velocity of the gas of $\approx 330\,{\rm km\,s^{-1}}$. This difference may be due to the passage of the SMBH itself; in the impulse approximation of de la Fuente Marcos & de la Fuente Marcos (2008), for example, the black hole imparts a velocity kick on the ambient gas. An intriguing alternative explanation is that the trajectory of the SMBH intersected gas that is not in virial equilibrium but an outflow or an inflow. An example of such a structure is a cold stream that could be funneling gas toward the galaxy. Such streams have been seen in simulations (Kereš et al. 2005; Dekel et al. 2009), although not yet observed. A cold stream could explain why the velocity dispersion of the gas is so low, and perhaps also facilitated raising the density above the threshold needed for gravitational collapse. It might also explain why the line-of-sight velocity at the location of the "counter" [O III] knot, on the other side of the galaxy, is much lower than the velocities along the primary wake, and perhaps also why no star formation is taking place on that side. We illustrate this possibility in the right panel of Fig. 7.

It is straightforward to improve upon the observations that are presented here. The main spectrum is a 30 min exposure with Keck/LRIS, and the exposure time for the near-IR spectrum that was used to measure [N II]/Hα was even shorter, 7.5 min. The extraordinary sensitivity of the red channel of LRIS enabled us to use the redshifted [O III] λ5007 line at $\lambda_{\rm obs} = 9834$ Å for most of the analysis, despite the short exposure time. Deeper data, for instance from the *JWST* NIRSPEC IFU, may show the expected broad, highly red- or blueshifted emission lines of ionized gas that is bound to the black holes themselves. Those data could also spatially resolve flows, shocks, and star formation near A (see Fig. 8). The HST data is similarly shallow, at 1 orbit for each of the two ACS filters. Deep ultraviolet imaging with UVIS is particularly interesting, as that could map the spatial distribution of shocked gas on both sides of the galaxy. A UVIS image would readily show whether the counter wake points to B or is precisely opposite the main wake. Finally, X-ray imag-

[2] We note that there is no appreciable contribution from emission lines in the HST filters; in particular, the redshifted [O III] doublet falls redward of the long wavelength cutoff of the F814W filter.

ing could further constrain the physics of the shock and the absorbing hydrogen column (see Dopita & Sutherland 1996; Wilson & Raymond 1999), or even directly detect the accretion disk of one or more of the SMBHs. The currently available 60 ks Chandra image shows no hint of a detection but as it is very far off-axis, there is room for improvement.

Looking ahead, the morphology of the feature in the HST images is so striking that it should not be too difficult to find more examples, if they exist. Future data from the Nancy Grace Roman telescope can be searched with automated algorithms; this is the kind of task that machine learning algorithms can be trained to do (see, e.g., Lochner & Bassett 2020). Although technically challenging, the most interesting wavelength to search in is probably the rest-frame far-UV, as it may include cases where the SMBH did not trigger star formation. Individual runaway SMBH systems are of great interest in their own right; furthermore, a census of escaped SMBHs can complement future gravitational wave measurements from LISA (Amaro-Seoane et al. 2017) for a complete description of SMBH evolution in – and out of – galaxy nuclei.

We thank the anonymous referee for their constructive and helpful report. Support from STScI grant HST-GO-16912 is gratefully acknowledged. S. D. is supported by NASA through Hubble Fellowship grant HST-HF2-51454.001-A.

REFERENCES

Allen, M. G., Groves, B. A., Dopita, M. A., Sutherland, R. S., & Kewley, L. J. 2008, ApJS, 178, 20, doi: 10.1086/589652

Amaro-Seoane, P., Audley, H., Babak, S., et al. 2017, arXiv e-prints, arXiv:1702.00786. https://arxiv.org/abs/1702.00786

Amorisco, N. C., Martinez-Delgado, D., & Schedler, J. 2015, arXiv e-prints, arXiv:1504.03697. https://arxiv.org/abs/1504.03697

Angus, C. R., Baldassare, V. F., Mockler, B., et al. 2022, Nature Astronomy, 6, 1452, doi: 10.1038/s41550-022-01811-y

Arp, H. C. 1972, in External Galaxies and Quasi-Stellar Objects, ed. D. S. Evans, D. Wills, & B. J. Wills, Vol. 44, 380

Bahcall, J. N., Kirhakos, S., Schneider, D. P., et al. 1995, ApJL, 452, L91, doi: 10.1086/309717

Baldwin, J. A., Phillips, M. M., & Terlevich, R. 1981, PASP, 93, 5

Begelman, M. C., Blandford, R. D., & Rees, M. J. 1980, Nature, 287, 307, doi: 10.1038/287307a0

Bekenstein, J. D. 1973, ApJ, 183, 657, doi: 10.1086/152255

Bicknell, G. V., Sutherland, R. S., van Breugel, W. J. M., et al. 2000, ApJ, 540, 678, doi: 10.1086/309343

Biretta, J. A., Sparks, W. B., & Macchetto, F. 1999, ApJ, 520, 621, doi: 10.1086/307499

Blandford, R. D., & Rees, M. J. 1974, MNRAS, 169, 395, doi: 10.1093/mnras/169.3.395

Blecha, L., Cox, T. J., Loeb, A., & Hernquist, L. 2011, MNRAS, 412, 2154, doi: 10.1111/j.1365-2966.2010.18042.x

Bonning, E. W., Shields, G. A., & Salviander, S. 2007, ApJL, 666, L13, doi: 10.1086/521674

Boylan-Kolchin, M., Ma, C.-P., & Quataert, E. 2004, ApJL, 613, L37, doi: 10.1086/425073

Brinchmann, J., Charlot, S., White, S. D. M., et al. 2004, MNRAS, 351, 1151, doi: 10.1111/j.1365-2966.2004.07881.x

Burbidge, E. M., Burbidge, G. R., Solomon, P. M., & Strittmatter, P. A. 1971, ApJ, 170, 233, doi: 10.1086/151207

Campanelli, M., Lousto, C. O., Zlochower, Y., & Merritt, D. 2007, PhRvL, 98, 231102, doi: 10.1103/PhysRevLett.98.231102

Chiaberge, M., Ely, J. C., Meyer, E. T., et al. 2017, A&A, 600, A57, doi: 10.1051/0004-6361/201629522

Chitan, A., Mylläri, A., & Valtonen, M. 2022, arXiv e-prints, arXiv:2205.04985. https://arxiv.org/abs/2205.04985

Choi, J., Dotter, A., Conroy, C., et al. 2016, ApJ, 823, 102, doi: 10.3847/0004-637X/823/2/102

Chun, S.-H., Yoon, S.-C., Jung, M.-K., Kim, D. U., & Kim, J. 2018, ApJ, 853, 79, doi: 10.3847/1538-4357/aa9a37

Civano, F., Elvis, M., Lanzuisi, G., et al. 2010, ApJ, 717, 209, doi: 10.1088/0004-637X/717/1/209

Coe, D. 2010, arXiv e-prints, arXiv:1005.0411. https://arxiv.org/abs/1005.0411

Conroy, C., Gunn, J. E., & White, M. 2009, ApJ, 699, 486, doi: 10.1088/0004-637X/699/1/486

Cramer, W. J., Kenney, J. D. P., Sun, M., et al. 2019, ApJ, 870, 63, doi: 10.3847/1538-4357/aaefff

Crockett, R. M., Shabala, S. S., Kaviraj, S., et al. 2012, MNRAS, 421, 1603, doi: 10.1111/j.1365-2966.2012.20418.x

Croft, S., van Breugel, W., de Vries, W., et al. 2006, ApJ, 647, 1040, doi: 10.1086/505526

Curti, M., Cresci, G., Mannucci, F., et al. 2017, MNRAS, 465, 1384, doi: 10.1093/mnras/stw2766

de la Fuente Marcos, R., & de la Fuente Marcos, C. 2008, ApJL, 677, L47, doi: 10.1086/587962

Dekel, A., Birnboim, Y., Engel, G., et al. 2009, Nature, 457, 451, doi: 10.1038/nature07648

Dopita, M. A., & Sutherland, R. S. 1995, ApJ, 455, 468

—. 1996, ApJS, 102, 161, doi: 10.1086/192255

Eldridge, J. J., Stanway, E. R., Xiao, L., et al. 2017, PASA, 34, e058, doi: 10.1017/pasa.2017.51

Escala, A., Larson, R. B., Coppi, P. S., & Mardones, D. 2005, ApJ, 630, 152, doi: 10.1086/431747

Fesen, R. A., Drechsler, M., Weil, K. E., et al. 2021, ApJ, 920, 90, doi: 10.3847/1538-4357/ac0ada

Foreman-Mackey, D., Hogg, D. W., Lang, D., & Goodman, J. 2013, PASP, 125, 306, doi: 10.1086/670067

Fragile, P. C., Anninos, P., Croft, S., Lacy, M., & Witry, J. W. L. 2017, ApJ, 850, 171, doi: 10.3847/1538-4357/aa95c6

Gaibler, V., Khochfar, S., Krause, M., & Silk, J. 2012, MNRAS, 425, 438, doi: 10.1111/j.1365-2966.2012.21479.x

Girelli, G., Pozzetti, L., Bolzonella, M., et al. 2020, A&A, 634, A135, doi: 10.1051/0004-6361/201936329

Graham, J. A. 1998, ApJ, 502, 245, doi: 10.1086/305888

Herrmann, F., Hinder, I., Shoemaker, D., Laguna, P., & Matzner, R. A. 2007, ApJ, 661, 430, doi: 10.1086/513603

Hills, J. G. 1988, Nature, 331, 687, doi: 10.1038/331687a0

Hoffman, L., & Loeb, A. 2007, MNRAS, 377, 957, doi: 10.1111/j.1365-2966.2007.11694.x

Ishibashi, W., & Fabian, A. C. 2012, MNRAS, 427, 2998, doi: 10.1111/j.1365-2966.2012.22074.x

Iwasawa, M., Funato, Y., & Makino, J. 2006, ApJ, 651, 1059, doi: 10.1086/507473

Jadhav, Y., Robinson, A., Almeyda, T., Curran, R., & Marconi, A. 2021, MNRAS, 507, 484, doi: 10.1093/mnras/stab2176

Keel, W. C., & Martini, P. 1995, AJ, 109, 2305, doi: 10.1086/117453

Keel, W. C., Chojnowski, S. D., Bennert, V. N., et al. 2012, MNRAS, 420, 878, doi: 10.1111/j.1365-2966.2011.20101.x

Kennicutt, R. C. 1998, ARA&A, 36, 189

Kereš, D., Katz, N., Weinberg, D. H., & Davé, R. 2005, MNRAS, 363, 2, doi: 10.1111/j.1365-2966.2005.09451.x

Kesden, M., Sperhake, U., & Berti, E. 2010, ApJ, 715, 1006, doi: 10.1088/0004-637X/715/2/1006

Kewley, L. J., Maier, C., Yabe, K., et al. 2013, ApJL, 774, L10, doi: 10.1088/2041-8205/774/1/L10

Komossa, S. 2012, Advances in Astronomy, 2012, 364973, doi: 10.1155/2012/364973

Komossa, S., Zhou, H., & Lu, H. 2008, ApJL, 678, L81, doi: 10.1086/588656

Lacy, M., Baum, S. A., Chandler, C. J., et al. 2020, PASP, 132, 035001, doi: 10.1088/1538-3873/ab63eb

Levesque, E. M., Massey, P., Olsen, K. A. G., et al. 2005, ApJ, 628, 973, doi: 10.1086/430901

Lintott, C. J., Schawinski, K., Keel, W., et al. 2009, MNRAS, 399, 129, doi: 10.1111/j.1365-2966.2009.15299.x

Lochner, M., & Bassett, B. A. 2020, Astronomaly: Flexible framework for anomaly detection in astronomy, Astrophysics Source Code Library, record ascl:2010.012. http://ascl.net/2010.012

Lousto, C. O., & Zlochower, Y. 2011, PhRvL, 107, 231102, doi: 10.1103/PhysRevLett.107.231102

Lousto, C. O., Zlochower, Y., Dotti, M., & Volonteri, M. 2012, PhRvD, 85, 084015, doi: 10.1103/PhysRevD.85.084015

Magain, P., Letawe, G., Courbin, F., et al. 2005, Nature, 437, 381, doi: 10.1038/nature04013

Mandal, A., Mukherjee, D., Federrath, C., et al. 2021, MNRAS, 508, 4738, doi: 10.1093/mnras/stab2822

Matthews, L. D., Gallagher, J. S., I., & van Driel, W. 1999, AJ, 118, 2751, doi: 10.1086/301128

Merritt, D., Schnittman, J. D., & Komossa, S. 2009, ApJ, 699, 1690, doi: 10.1088/0004-637X/699/2/1690

Merritt, D., Storchi-Bergmann, T., Robinson, A., et al. 2006, MNRAS, 367, 1746, doi: 10.1111/j.1365-2966.2006.10093.x

Milosavljević, M., & Merritt, D. 2001, ApJ, 563, 34, doi: 10.1086/323830

Mould, J. R., Huchra, J. P., Freedman, W. L., et al. 2000, ApJ, 529, 786, doi: 10.1086/308304

Oke, J. B., & Schmidt, M. 1963, AJ, 68, 288, doi: 10.1086/109103

Oke, J. B., Cohen, J. G., Carr, M., et al. 1995, PASP, 107, 375, doi: 10.1086/133562

Pello, R., Le Borgne, J.-F., Soucail, G., Mellier, Y., & Sanahuja, B. 1991, ApJ, 366, 405, doi: 10.1086/169574

Peng, C. Y., Ho, L. C., Impey, C. D., & Rix, H.-W. 2002, AJ, 124, 266, doi: 10.1086/340952

Pillepich, A., Springel, V., Nelson, D., et al. 2018, MNRAS, 473, 4077, doi: 10.1093/mnras/stx2656

Prochaska, J., Hennawi, J., Westfall, K., et al. 2020, The Journal of Open Source Software, 5, 2308, doi: 10.21105/joss.02308

Rees, M. J. 1989, MNRAS, 239, 1P, doi: 10.1093/mnras/239.1.1P

Rees, M. J., & Saslaw, W. C. 1975, MNRAS, 171, 53, doi: 10.1093/mnras/171.1.53

Ricarte, A., Tremmel, M., Natarajan, P., & Quinn, T. 2021a, ApJL, 916, L18, doi: 10.3847/2041-8213/ac1170

Ricarte, A., Tremmel, M., Natarajan, P., Zimmer, C., & Quinn, T. 2021b, MNRAS, 503, 6098, doi: 10.1093/mnras/stab866

Robinson, A., Young, S., Axon, D. J., Kharb, P., & Smith, J. E. 2010, ApJL, 717, L122, doi: 10.1088/2041-8205/717/2/L122

Román, J., Castilla, A., & Pascual-Granado, J. 2021, A&A, 656, A44, doi: 10.1051/0004-6361/202142161

Sahu, K. C., Anderson, J., Casertano, S., et al. 2022, ApJ, 933, 83, doi: 10.3847/1538-4357/ac739e

Salomé, Q., Salomé, P., & Combes, F. 2015, A&A, 574, A34, doi: 10.1051/0004-6361/201424932

Sambruna, R. M., Maraschi, L., Tavecchio, F., et al. 2002, ApJ, 571, 206, doi: 10.1086/339859

Saslaw, W. C., & De Young, D. S. 1972, Astrophys. Lett., 11, 87

Saslaw, W. C., Valtonen, M. J., & Aarseth, S. J. 1974, ApJ, 190, 253, doi: 10.1086/152870

Schutte, Z., Reines, A. E., & Greene, J. E. 2019, ApJ, 887, 245, doi: 10.3847/1538-4357/ab35dd

Shapley, A. E., Reddy, N. A., Kriek, M., et al. 2015, ApJ, 801, 88, doi: 10.1088/0004-637X/801/2/88

Shull, J. M., & McKee, C. F. 1979, ApJ, 227, 131, doi: 10.1086/156712

Silk, J. 2013, ApJ, 772, 112, doi: 10.1088/0004-637X/772/2/112

Smith, D. J. B., Krause, M. G., Hardcastle, M. J., & Drake, A. B. 2022, MNRAS, 514, 3879, doi: 10.1093/mnras/stac1568

Steidel, C. C., Rudie, G. C., Strom, A. L., et al. 2014, ApJ, 795, 165, doi: 10.1088/0004-637X/795/2/165

Sutherland, R. S., Bicknell, G. V., & Dopita, M. A. 1993, ApJ, 414, 510, doi: 10.1086/173099

Tran, H. D., Sirianni, M., Ford, H. C., et al. 2003, ApJ, 585, 750, doi: 10.1086/346125

Uchiyama, Y., Urry, C. M., Cheung, C. C., et al. 2006, ApJ, 648, 910, doi: 10.1086/505964

Ueda, Y., Hashimoto, Y., Ichikawa, K., et al. 2015, ApJ, 815, 1, doi: 10.1088/0004-637X/815/1/1

Valtonen, M., & Mikkola, S. 1991, ARA&A, 29, 9, doi: 10.1146/annurev.aa.29.090191.000301

van der Wel, A., Franx, M., van Dokkum, P. G., et al. 2014, ApJ, 788, 28, doi: 10.1088/0004-637X/788/1/28

van Dokkum, P., Shen, Z., Keim, M. A., et al. 2022a, Nature, 605, 435, doi: 10.1038/s41586-022-04665-6

van Dokkum, P., Shen, Z., Romanowsky, A. J., et al. 2022b, ApJL, 940, L9, doi: 10.3847/2041-8213/ac94d6

Volonteri, M., Haardt, F., & Madau, P. 2003, ApJ, 582, 559, doi: 10.1086/344675

Walmswell, J. J., Tout, C. A., & Eldridge, J. J. 2015, MNRAS, 447, 2951, doi: 10.1093/mnras/stu2666

Whitaker, K. E., Franx, M., Leja, J., et al. 2014, ApJ, 795, 104, doi: 10.1088/0004-637X/795/2/104

Wilson, A. S., & Raymond, J. C. 1999, ApJL, 513, L115, doi: 10.1086/311923

Zovaro, H. R. M., Sharp, R., Nesvadba, N. P. H., et al. 2019, MNRAS, 484, 3393, doi: 10.1093/mnras/stz233